The Sub-Parsec-Scale Structure and Evolution of Centaurus A – the Nearest Active Radio Galaxy

S.J. Tingay

California Institute of Technology, Jet Propulsion Laboratory, MS238-332, 4800 Oak Grove Drive, Pasadena, CA 91109

tingay@hyaa.jpl.nasa.gov

D.L. Jauncey, J.E. Reynolds, A.K. Tzioumis, and E.A. King

CSIRO, Australia Telescope National Facility, P.O. Box 76, Epping, NSW 2121, Australia

(djauncey,jreynold,atzioumi,eking)@atnf.csiro.au

R.A. Preston, D.L. Jones, D.W. Murphy, D.L. Meier, and T.D. van Ommen

California Institute of Technology, Jet Propulsion Laboratory, MS238-332, 4800 Oak Grove Drive, Pasadena, CA 91109

rap@sgra.jpl.nasa.gov,dj@bllac.jpl.nasa.gov,dwm@casa.jpl.nasa.gov,dlm@cena.jpl.nasa.gov

P.M McCulloch, S.P. Ellingsen, and M.E. Costa

University of Tasmania, G.P.O. Box 252C, Hobart, Tasmania 7001, Australia

pmcc@physvax.phys.utas.edu.au,sellingsen@kerr.phys.utas.edu.au,mcosta@kerr.phys.utas.edu.au

P.G. Edwards, J.E.J. Lovell

Institute of Space and Astronautical Science, 3-1-1, Yoshinodai, Sagamihara-shi, Kanagawa 229, Japan

pge@orihime.isaslan1.isas.ac.jp, jlovell@vsop.isas.ac.jp

G.D. Nicolson, J.F.H. Quick, and A.J. Kemball

Hartebeesthoek Radio Astronomy Observatory, P.O. Box 443, Krugersdorp 1740, Transvaal, South Africa

george@bootes.ac.za

V. Migenes

National Astronomical Observatory, Mitaka-shi, Tokyo 181, Japan

migenes@hotaka.mtk.nao.ac.jp

P. Harbison

British Aerospace Australia, Canberra, ACT, Australia

P.A. Jones and G.L. White

University of Western Sydney, Kingswood, NSW, Australia

R.G. Gough, R.H. Ferris, and M.W. Sinclair

CSIRO, Australia Telescope National Facility, P.O. Box 76, Epping, NSW 2121, Australia

R.W. Clay

University of Adelaide, Adelaide, SA, Australia

Received _____; accepted _____

ABSTRACT

We present high-resolution VLBI radio images of the closest classical radio galaxy, Centaurus A, including the highest resolution image yet for this source. The images were made from data obtained over a period of approximately 8 yr at the frequencies of 2.3, 4.8, and 8.4 GHz with the Southern Hemisphere VLBI Experiment (SHEVE) array and at 2.3, 8.4, and 22.2 GHz with the VLBA. We give complete details of the data reduction and analysis procedures.

The sub-parsec-scale structure of Centaurus A is complex, consisting of a bright jet and a fainter counterjet. The bright jet contains components which have sub-luminal speeds of approximately 0.1c and undergo irregular episodes of rapid internal evolution. The rapid evolution sometimes observed could be interpreted as evidence for an underlying jet flow much faster (>0.45c) than observed from the proper motion of components (~0.1c). Considering the large-scale morphology of the source, the motions and temporal variations in the jet, and the detection of a counterjet, we conclude that the axis of the Centaurus A jet lies between ~50° and ~80° to our line of sight.

We find that the estimated times of component ejection from the compact core are reasonably coincidencent with enhancements in hard X-ray intensity and 22 GHz flux density.

In the context of the radio-galaxy population Centaurus A is a low-luminosity FR-I-type source and in general has the properties observed in other FR-I radio galaxies. Overall, the observations of Centaurus A presented here, and from other investigations, are consistent with the idea that sources with an FR-I appearance are not aligned with our line of sight and have relativistic flow on the sub-parsec scale. The apparently sub-luminal sub-parsec-scale jet components are interpreted as being slow patterns on the relativistic flow.

Subject headings: Galaxies: Active, Individual (NGC 5128, Centaurus A, PKS 1322−427) – Radio Continuum: Galaxies – Methods: Interferometric

1. INTRODUCTION

Centaurus A (PKS 1322–427, NGC 5128) is the closest classical radio galaxy, at a distance of approximately 3.5 Mpc (Hui et al. 1993). It was one of the first radio sources to be identified with an extragalactic object (Bolton, Stanley, and Slee 1949) and is one of the brightest extragalactic radio sources in the sky with an integrated flux density of 681 ± 34 Jy at a wavelength of 6 cm (Junkes et al. 1993). Its proximity offers excellent spatial resolution at the source in return for high angular resolution observations; 1 mas corresponds to approximately 24 light days and 1″ corresponds to approximately 20 pc. Including the results presented in this paper, Centaurus A/NGC 5128 has been observed over eight orders of magnitude in spatial scale and 12 orders of magnitude in photon energy (Odenwald, Gehrels, and Howard 1994).

The entire radio source occupies approximately 3.5° × 8.5° on the sky, including the faint extended emission which is oriented along a position angle of approximately 0° (Junkes et al. 1993; Combi and Romero 1997). Straddling the optical galaxy along a position angle of approximately 50° and separated by approximately 15 kpc are two lobes of radio emission which have been imaged in detail with the VLA (Clarke, Burns, and Norman 1992). An unresolved and inverted spectrum radio core which is coincident with the center of the optical galaxy is connected to the north-east lobe by a radio jet (Burns, Fiegelson, and Schreier 1983). The jet is obscured at optical wavelengths but has been detected at infrared (Joy et al. 1991) and X-ray (Döbereiner et al. 1996) wavelengths.

VLBI observations of Centaurus A are aimed at imaging the inverted spectrum radio core. Wade et al. (1971) undertook the first high resolution radio observations of Centaurus A and reported a source less than 0.″5 in extent, although noting that the inverted spectrum of the core implied a much smaller extent. Using VLBI observations, Preston et al. (1983) suggested a model for the nuclear radio source in Centaurus A which

consisted of two components, a 50 mas jet which was seen with 2.3 GHz observations, and a more compact component likely to be the core, seen only at higher frequencies since it is severely self-absorbed at lower frequencies. Based on 2.3 and 8.4 GHz VLBI observations of Centaurus A that were undertaken during the first SHEVE (Southern Hemisphere VLBI Experiment) observing session in 1982, Meier et al. (1989) proposed a model for the source which consisted of a weak self-absorbed core and an extended jet component some 100 mas away which can be seen at both frequencies; the core-jet position angle was estimated to be $51°\pm3°$, in agreeing with the jet position angle from VLA images of the kiloparsec-scale radio structure.

In this paper we present detailed multi-frequency VLBI images of the sub-parsec-scale structure of Centaurus A. The observations span more than 8 yr and use both the SHEVE array and the VLBA. Using a long series of VLBI observations at 8.4 GHz, we develop a detailed model for the structure and evolution of the source. We also compare these results with multiwavelength monitoring observations of Centaurus A by other investigators, in particular the 22 GHz flux density monitoring of Botti & Abraham (1993) and the hard X-ray monitoring of Morini et al. (1989), Bond et al. (1996) and Kinzer et al. (1995).

2. DATA REDUCTION AND ANALYSIS

2.1. Observations

Table 1 lists our VLBI observations of Centaurus A between 1988 and 1996. All of the data were recorded with single circular polarizations according to IEEE convention and at the standard global network observing frequencies at 2.3 GHz (RCP), 4.8 GHz (LCP), 8.4 GHz (RCP), and 22.2 GHz (LCP).

All of the VLBA observations using the VLBA recording format were made with an

aggregate bit rate of 128 Mb s^{-1}, 1-bit sampling, and a 64 MHz band broken into eight IFs, except for the observations of 95/07/03 where four of the eight IFs were at 2.3 GHz and the remaining four IFs were at 8.4 GHz, giving simultaneous dual-frequency data. All of the Mark III observations were made with upper and lower sidebands of 2 MHz at seven IFs, giving a total recorded bandwidth of 28 MHz. All of the Mark II observations used upper sideband and a 2 MHz bandwidth.

2.2. Correlation and fringe-fitting

All VLBA data recorded in VLBA mode were correlated at the VLBA processor in Socorro. The resulting data were read directly into AIPS and reduced and fringe-fitted using the method recommended in the AIPS cookbook. This reduction path includes fringe-fitting with the task FRING. Up until the epoch of 96/03/23 all of our VLBA format data reduced in this way required manual calibration for instrumental effects such as channel phase offsets and single-band delays. After and including the 96/03/23 observations, the initial instrumental calibrations were available from the observation log file.

The Mark III data recorded during the 92/11/22 observation were correlated at the Mark III processor of the US Naval Observatory in Washington D.C. (the data from the correlator were exported to us after being fringe-fitted). All other Mark III data were correlated as global experiments at the VLBA processor in Socorro and fringe-fitted according to the suggested reduction path in the AIPS cookbook.

All the Mark II data were correlated by us at the JPL/Caltech Block II processor in Pasadena. Initially we examined the correlated data for calibrator sources observed at each epoch, over a wide range in delay (64 μs) on baselines to a reference antenna, in order to find the fringes and determine clock offsets and rates at each station. For much of the

SHEVE data this is an important step since some of the antennas were equipped with Rubidium clocks, which commonly have high drift rates and can undergo frequent clock jumps. After determining the behavior of the clocks and adding that information to the correlator model, the data could be correlated on all baselines simultaneously with a much smaller delay window of 2 μs. The data from the final correlations were exported into AIPS as a FITS file and fringe-fitted using the task FRING.

Once the fringe-fitted and frequency-averaged data were available from each set of observations, the visibility data were self-calibrated with a point-source model to straighten the phases. The data were then averaged coherently with time to produce one visibility point per 60 s, reducing the datasets to manageable sizes.

2.3. Amplitude calibration

For all of the data before and including 95/07/03 the FITS format visibility file output from fringe-fitting in AIPS was converted to a MERGE format file for use with the Caltech VLBI reduction package (Pearson 1991). The available system temperatures, correlator B factors, nominal antenna sensitivities, and gain-elevation curves for each dataset were used to produce files in the format suitable for the Caltech task CAL. Using CAL, the amplitude calibration information was applied to nearly unresolved calibrator sources from the same observing session as the Centaurus A observations. The visibility amplitudes of the calibrators were then examined and compared from baseline to baseline. Usually, the baseline amplitudes were within 10% of each other. Occasionally, however, the baselines to a particular antenna were very different to the rest of the baselines in a dataset. This was usually caused by a change in one of the antenna sensitivities away from the nominal value. In these cases a single amplitude self-calibration was performed on the calibrator source to obtain a correction to the *a priori* calibration data. The corrected calibration was then

applied to the Centaurus A data. If the uncorrected amplitudes of calibrator sources were consistent to within 10% on all baselines, the *a priori* calibrations were applied directly to the Centaurus A data.

For data obtained after 95/07/03 (all from the VLBA in VLBA format) the amplitude calibration was applied to the data before fringe-fitting, with the AIPS tasks ANTAB and APCAL. After fringe-fitting and averaging in frequency and time, the amplitude scale was checked by examining plots of amplitude versus $u - v$-distance for both calibrator sources and Centaurus A itself. For both Centaurus A and the calibrator sources the baseline amplitudes were never discrepant by more than 10%.

2.4. Imaging

All of the VLBI data, once averaged in frequency and time and amplitude calibrated, were imaged using the DIFMAP software (Shepherd, Pearson, and Taylor 1993). Initially, phase-only self-calibration was used in conjunction with a tight clean window on the brightest region of the source. In subsequent clean–self-calibrate iterations the clean windows were extended to include fainter emission although, still, only the phases were self-calibrated. Finally, when the flux density of the clean model reached the level of the amplitudes on the shorter baselines, amplitude self-calibration was performed initially with a time-scale much longer than the observation length and subsequently on shorter time-scales, until point-to-point amplitude self-calibration was performed.

It should be noted that at three epochs, 92/11/22, 93/07/03, and 93/10/20, both Mark II and Mark III data were available. Once correlated, fringe-fitted, averaged, and calibrated, the Mark II and Mark III datasets were combined using the Caltech package task MERGE.

The signal-to-noise ratio of the VLBA Mark III and SHEVE Mark II data were well

matched since the wide bandwidth of the Mark III observations was balanced by the use of large antennas (Tidbinbilla, 70 m; Parkes, 64 m) to anchor the SHEVE Mark II array. Also the amplitude calibrations of the two separate arrays agreed to better than 10% with no discernible systematic offset between the two.

The combined data gave $u - v$ coverages which were far superior to those from either of the individual arrays alone, the east-west baselines of the VLBA supplementing the north-south baselines of the SHEVE array. The combined data were imaged as outlined above.

3. RESULTS

3.1. The maps

The maps resulting from the imaging procedure are shown in frequency order in Figure 1. (Images from the combined SHEVE and VLBA epochs are shown in Figures 1h, 1j, and 1l.) Table 2 lists relevant parameters of the maps.

Limited results from the nearly coeval 8.4 and 4.8 GHz observations of 92/11/22 and 92/11/25, which unambiguously identify the compact core of Centaurus A, have been published previously (Jauncey et al. 1995). The core appears in the 8.4 GHz images as the bright, compact component at the south-west end of the jet.

The core is self-absorbed (Jauncey et al. 1995; Jones et al. 1996) and therefore is not visible in the 2.3 GHz images of Figure 1. Registration of the 2.3 and 8.4 GHz images is done via a prominent "kink" in the jet, as described in Jones et al. (1996). These images are discussed in more detail in §4.2. The core is only weakly seen in the 4.8 GHz images. The phase center in the 2.3 and 4.8 GHz maps coincides with the brightest feature in the source at this frequency, which lies mid-way along the jet.

It is the long series of 8.4 GHz images, in which the core is the dominant feature, that provide the best opportunity to quantify the sub-parsec-scale structure and evolution of Centaurus A, and this is undertaken in the next Section. A montage of all the 8.4 GHz images with similar resolution is shown in Figure 2. The solid lines superposed on Figure 2 are discussed in §3.3. Finally, the 22 GHz image shown in Figure 1u is the highest resolution image obtained to date of this source. It is discussed further in §3.3.

3.2. Quantifying the sub-parsec-scale structure of Centaurus A

To quantify the sub-parsec-scale structure of Centaurus A, using its compact core as our reference point in the image plane, we analyzed of the VLBI data using the Caltech VLBI package task MODELFIT (Pearson 1991). MODELFIT uses a nonlinear least-squares algorithm to fit the parameters of a set of simple components in the image plane (a model) to the visibility amplitudes and closure phases of the VLBI data, and reports a measure of the goodness-of-fit (defined as the square root of the reduced chi-squared value for the fit of model to data). The best-fitting model is the one which minimizes the reduced chi-squared value.

To begin model-fitting an initial model must be chosen. We used a model which consisted of components representing the major features that could be seen in the 8.4 GHz images: a bright, compact component at the south-west end of the source which represents the core, a component approximately 8 - 10 mas away from this component at a position angle of approximately 51° (designated C2), and a component approximately 15 - 20 mas away from the core at the same position angle (designated C1).

MODELFIT was then run using this initial model and the self-calibrated visibility data from 13 of the 16 8.4 GHz images (the three images produced from the combined SHEVE

and VLBA u-v coverage were excluded because the high-resolution visibilities were too complex to fit the model meaningfully). When MODELFIT completed fitting the model to data at a given epoch, the data were compared to the model, to determine if the model was a good representation of the data. At every epoch the simple model did not fit the data well. Guided by the images once again, a further component was added to each initial model and MODELFIT was attempted once again.

At 8 of the 13 epochs, the visibility data were well fitted by four-component models in this way. For the remaining five epochs four-component models did not fit well but five-component models did. Table 3 contains lists of the model components used at each epoch.

The core component appears strongly in each of the models. The component C2 can also be identified in the models at each epoch. The component C1 can be identified at 11 of the 13 epochs in the models. At two epochs, 91/11/24 and 93/10/20, it is not clear which, if any, of the model components corresponds to C1. In the last 8 epochs, an additional component can be identified between the core and C2 in the models, and is designated C3. Lastly, at 8 of the 13 epochs one or more of the components in the models have been identified as possible or definite jet-like components. These components are often required by the data to take an extended (elongated along the jet) and diffuse appearance, with a constant surface brightness over their extent, in contrast to the discrete Gaussian components C1, C2, and C3. Such a jet-like component was first noted by Meier et al. (1989) in their model of the first 8.4 GHz VLBI observations of Centaurus A. This component probably represents the underlying, smooth emission from the jet.

It should be noted that the jet component in 91/03/06 is somewhat in question, since only four telescopes were available at that epoch. The component identified as the possible jet is a Gaussian and therefore may be a true discrete component, possibly part of C1.

However, given the lack of telescopes at this epoch and the consistency of the overall data, we feel that the most plausible explanation for this component is that it is the extended jet, truncated by the lack of $u - v$ coverage in the observation.

3.3. Quantifying the sub-parsec-scale evolution in Centaurus A

The ultimate aim of the model-fitting analysis was to quantify the evolution of the components in the source. To achieve this aim further analyses of the models were undertaken to estimate the errors on the best-fitting parameters at each epoch. The model-fitting errors are required to determine whether or not the differences between the models at each epoch are significant.

To estimate errors, the best-fitting model at a given epoch and its corresponding dataset were taken back into the MODELFIT program. The best-fitting value for a single parameter of a given component in the model was then altered by a small (typically 5 - 10% of the value of the parameter) amount and fixed at the new value. MODELFIT was then allowed to re-converge the model with all parameters varying, except for the parameter which had been fixed and the position of the core. When the model had re-converged to its new goodness-of-fit (worse than for the best-fitting model), its fit to the visibility amplitudes and closure phases was compared to the fit of the best-fitting model. The Caltech VLBI task VPLOT was used to plot the data against the model predictions and a visual comparison of the two fits was made. If no significant difference could be found between the fit of the two models then the process was repeated, after the parameter being considered had been fixed again at a new, larger displacement from its best-fitting value. This process allowed us to see how far from best-fit we could force certain components of the models, while the model as a whole retained a good fit to the data.

When a displacement was reached at which the fit of the re-converged model to the data was significantly worse than for the best-fitting model, the displacement defined the error bar in one direction. Displacements in the opposite sense were used to define the error bar in the opposite direction.

The comparison of model fits was necessarily a subjective one. However, several ground rules were established for the purpose of deciding whether a difference between fits was significant or not. First, none of the fits was perfect, there were differences between model and data on some baselines and closure triangles in every data set. The baselines and closure triangles which were very well fitted by the best-fitting model were most closely monitored in the error-determination process. The fit was deemed to be significantly worse than the best-fitting model if the model prediction was outside the scatter in the visibilities for periods longer than 2 hr on two or more baselines and/or closure triangles which were well fitted by the best-fitting model, and if further steps away from the best-fitting solution caused even greater divergence from the data. Otherwise any differences in the fits were deemed not significant.

This method can be applied to any of the parameters in the models. However, the analysis was most successful in its application to the core-component separations for the discrete components in the source, namely C1, C2, and C3. For example, from an analysis of the errors on the flux densities of individual components it became clear that the various components in a given model were easily able to "trade" flux density in a way which satisfied the MODELFIT program over a large range in displacement from best-fittiing values, giving no useful estimate of the errors. The core-component separations for the discrete components were the best constrained parameters, probably because the closure-phase information maintained a strong influence.

Figure 3 presents the results of the model-fitting error analysis for the core-component

separations of C1, C2, and C3, showing the dependence of the model-fitting error results on the form of the model. In the early epochs, when the component C2 was very bright, small, and close to the core, the errors on the position of C2 are small because the model was relatively simple and fitted the data very well. Small deviations from the best-fitting model disagreed significantly with the data. However, as time passed and C2 evolved, becoming larger and weaker, the error on its position increased, especially after the time at which C3 was ejected from the core. The more complex model involving more parameters agreed with the data over a wider range in displacements from the best-fitting position. Over the entire 5.3 yr period of monitoring, however, Figure 3 shows that components C1 and C2 have significantly changed their positions relative to the core. A linear least-squares fit of a constant separation speed to the series of core-C2 separations gives an angular motion for C2 relative to the core of $1.7^{+0.5}_{-0.2}$ mas yr^{-1} corresponding to an apparent speed of β_{app}=v$_{app}$/c=$0.11^{+0.03}_{-0.01}$, with small residuals at most epochs (mean deviation from fit is 0.5 mas with a standard deviation of 0.6 mas). Extrapolating the motion back in time gives a core-C2 zero separation time of $1989.2^{+0.9}_{-0.7}$.

A similar linear least-squares fit to the core-C1 separations gives an angular motion for C1 relative to the core of 2.0 ± 0.4 mas yr^{-1}, corresponding to β_{app}=v$_{app}$/c=0.13 ± 0.03, giving a core-C1 zero separation time of $1983.5^{+2.2}_{-3.2}$. However, the residuals on this fit are larger than for C2 at most epochs (mean deviation from fit is 1.2 mas with a standard deviation of 0.8 mas) and it may be that a single, constant expansion speed may not be the best description for the evolution of this component. In Figure 2 the solid lines superposed onto the 8.4 GHz montage represent the linear least-square fits to the C1 and C2 data shown in Figure 3. In addition the position of the core component is marked.

From the visibility data, the images, and the models, it is apparent that C1 undergoes strong internal evolution. Over the period of the first three epochs (91/03/06 to 92/03/26)

C1 changed its structure appreciably, from being a discrete component at 91/03/06 (see images and model) to being possibly absent from the source model at 91/11/24, and returning as a bright and discrete component some time during the following 4 months to 92/03/26 (see also Meier et al. 1993; Tingay et al. 1994; Preston et al. 1996). The evolution between 91/11/24 and 92/03/26 could be characterized by the appearance of a component within C1 approximately 0.3 ly (4.5 mas) in projected extent (from a comparison of the models) over the 0.34 yr period (Figure 4). Alternatively, the two sub-components which appear to make up the C1 component at 91/11/24 may have moved together over the 0.34 yr period to form a single component at 92/03/26. If this is the case then each sub-component would have had to have moved a projected distance of 0.2 – 0.3 ly in the 0.34 yr period.

Also between the epochs of 92/11/22 and 93/10/20, C1 altered its appearance considerably. C1 appears to have increased its separation from the core by approximately 0.4 ly (6 mas) over the 0.9 yr period, remaining close to that separation until the end of the series of observations. Thus, the behavior of C1 could be accounted for by a slow, linear motion combined with internal changes on much shorter time-scales.

The component C3 was detected only in the data starting at the 93/10/20 epoch, and the error bars do not indicate any significant motion, $\beta_{app}=v_{app}/c=0.04 \pm 0.1$. If a separation speed identical to that for C2 is assumed, then the core-C3 zero separation time was between 1992 and 1993. The component C3 is clearly seen $\sim$5.5 mas from the core in the 22 GHz image (Figure 1u), and this separation is well within the error bars of Figure 3.

4. DISCUSSION AND CONCLUSIONS

4.1. Structure and flux density variability

On the sub-parsec scale Centaurus A is a complex core-jet source. Our model-fitting analyses of the 8.4 GHz VLBI data have shown that three main discrete components lie within the jet (C1, C2, and C3), to the north-east of the core and are moving with apparent sub-luminal speeds of the order of approximately 0.1c. However, in one component, C1, which is the largest and most distant from the core of the three, we see evidence for internal evolution on short time-scales; C1 appeared to change its internal structure dramatically near two epochs, 91/11/24 and 93/07/03.

The behavior of C1 is difficult to interpret since the epochs of observation have under-sampled the episodes of rapid evolution and the angular resolution of the observations does not allow us to probe C1 in fine detail. However, two simple interpretations were put forward in §3.3, the rapid brightening of a discrete region of C1 (applicable between 91/11/24 - 92/03/26) or the rapid motion of sub-components in C1 (applicable between 91/11/24 and 92/03/26 and between 92/11/22 and/or 93/10/20).

Between 91/11/24 and 92/03/26, if the first of the two interpretations is used and the brightening of C1 is attributed to the advance of jet material through the component, then the brightening of a 0.3 ly (projected) region in <0.34 yr implies an apparent jet speed of >0.90 c. If the second interpretation is used and the two sub-components at 91/11/24 were in motion in such a way as to come together to form a single component at 92/03/26 then 0.2 – 0.3 ly (projected) was traversed by each sub-component in <0.34 yr, corresponding to apparent speeds of >0.60 c.

Between 92/11/22 and 93/10/20, if the second interpretation is used and the component C1 has shifted by 0.4 ly (projected) in <0.9 yr, then an apparent speed of >0.45 c can be

inferred. Each of these interpretations is uncertain, but all point to speeds much larger than measured from the gradual separation of the component C2 from the core.

The parsec-scale structural variability in Centaurus A can also be compared to the total flux density light curves at 22 GHz of Botti & Abraham (1993) and the hard X-ray data of Morini et al. (1989), Kinzer et al. (1995) and Bond et al. (1996).

The estimated zero separation times for C1, C2 , and C3 are $1983.5^{+2.2}_{-3.2}$, $1989.2^{+0.9}_{-0.7}$, and 1992 - 1993, respectively. The 22 GHz light curve of Botti & Abraham (1993) over the period from 1984 to 1992 is characterized by a gradual decline in flux density, superimposed with low-amplitude, fast variations. A dramatic outburst in flux density, from 20 Jy to 30 Jy and back to 20 Jy, occurred over two months around 1985.7, suggesting a match to the core-C1 zero separation time. There is no significant 22 GHz flux density variation apparent at the core-C2 zero separation time, although Botti & Abraham (1993) point out that outbursts on such short time-scales could have been easily missed due to under-sampling. No 22 GHz monitoring data are available to compare against the core-C3 zero separation time. The highest flux density in the 90 GHz monitoring of Tornikoski et al. (1996) between 1990.2 and 1994.5 was recorded in 1993.2, but the large gaps in the monitoring (no measurements were made in 1991) and the uncertainty in the speed of C3 prevent any conclusions being drawn about a correlation for that component. No significant variations can be seen during the periods of rapid evolution in the component C1.

Bond et al. (1996) present a light curve summarizing X-ray observations of Centaurus A spanning the period of our 8.4 GHz VLBI observations. From the light curve, three enhancements in hard X-ray intensity are apparent near 1985.5, 1988.5–1989.5, and 1991.5. These times agree reasonably well with the core-component zero separation times, and the 1985.7 22 GHz flux density outburst, suggesting that components are ejected from the core accompanied by an enhancement in hard X-ray flux and perhaps an outburst at

radio wavelengths. The sparseness of the X-ray light curve and the uncertainties in our estimated zero-separation times suggest, rather than compel, the match between the X-ray enhancements and component ejections.

It is also possible that some of the variation in hard X-rays could be identified with the short time-scale internal variability in the C1 component, in particular the 1991.5 X-ray enhancement with the 91/11/24 – 92/03/26 C1 episode. However, this is not likely since Bond et al. (1996) have constrained the size of the X-ray emission region to be $< 10^{16}$ cm in extent. C1 has a measured angular size ranging between 4 and 14 mas, corresponding to $> 2 \times 10^{17}$ cm. The only component in Centaurus A with a size comparable to 10^{16} cm is the core; Kellermann, Zensus, & Cohen (1997) measured a size of 0.01pc $\sim 3 \times 10^{16}$ cm with the VLBA at 43 GHz. Thus the core component is the likely source of hard X-rays, not components in the sub-parsec-scale jet.

We have established that at least two of the three components in the jet of Centaurus A show evidence for motion. We can also examine evolution in the flux density of the components.

The 8.4 GHz flux densities of the four compact components in the images, derived from the model-fitting analyses, are plotted in Figure 5. There is an uncertainty of ~10% in the flux density calibration of our VLBI observations, which is not shown. It should also be noted that, as indicated in Table 3, the shape and size of the component determined from the model-fitting procedures varies from epoch to epoch. Nevertheless, a number of conclusions can be drawn from the figure.

The core has remained relatively stable in strength over a 6 yr period. C3 has also shown little evolution in flux density since its ejection.

However, significant variation in the model-fitted flux density of C1 is evident over the

first four epochs. The sizes of the fitted components is significantly larger at the two epochs of higher flux density, coinciding with the epochs of significant structural evolution, and possible explanations for these variations have been considered in §3.3. After this period of activity the flux density declined and from 94/06/20 onwards has remained relatively constant.

The behavior of component C2 is much simpler. Its brightness decreased by a factor of ~3 over the first two years, and has remained relatively constant since. An extrapolation of its motion reveals that during 1998 it will reach a similar distance from the core to that where C1 underwent dramatic variation. If C2 were to show similar activity at that time, it would suggest the presence of an underlying feature in the jet such as a quasi-stationary shock, responsible, perhaps, for both the structural and flux density variability we have observed on the sub-parsec scale.

4.2. The sub-parsec-scale counterjet

The discovery of the sub-parsec-scale counterjet in Centaurus A has been reported previously (Jones et al. 1996). The counterjet has been detected at two frequencies, 2.3 GHz (Figures 1a and 1b) and 8.4 GHz (Figures 1h, 1j, and 1l) with three different array configurations (Table 1). The counterjet components are discrete and no smooth extended component is evident underlying these components; they are also faint compared to the emission of the main jet. Thus, it is not surprising that the counterjet is detectable in our data only when it is observed at our lowest frequency (2.3 GHz) or when we have the most sensitive arrays (combined SHEVE and VLBA). At some other epochs, even though the counterjet is not seen sufficiently well to be included as part of the clean component model, the brightest residual flux in the image appears on the counterjet side of the core (Figures 1k, 1m, 1o, 1q, and 1r). The counterjet was not detected at 4.8 GHz because the lack of

telescopes and the long baselines used allowed us to image the brightest emission only at this frequency reliably, the main jet.

Future observations which combine the SHEVE and VLBA arrays will be required to gain images with good resolution and high sensitivity, like Figure 11. If the motion of components in the counterjet is similar to the jet components then only a few years of observations will be required to measure their apparent speeds accurately.

Jones et al. (1996) found the jet-to-counterjet surface brightness ratio, R, for Centaurus A on the sub-parsec-scale to be between 4 and 8, assuming intrinsically identical, oppositely directed jets,

$$R = \left(\frac{1 + \beta cos\theta}{1 - \beta cos\theta} \right)^{3-\alpha} . \quad (1)$$

Here, α is the spectral index of the jet emission and θ is the angle between the jet and the line of sight; $3 - \alpha$ was chosen as the exponent for this calculation since it is appropriate for a spherical plasmoid rather than $2 - \alpha$ for a smooth jet. We have detected the jet at two frequencies at the same epoch, but cannot accurately constrain the spectral index since it is likely that free-free absorption is strongly affecting the observed spectral index (Jones et al. 1996). However, the slow speed measured for C2 is inconsistent with a surface brightness ratio in the range 4 - 8, if optically thin synchrotron emission from the jet, $\alpha = -0.6$, is assumed. On the other hand, under the same spectral index assumption, the interpretation-dependent speeds inferred from the rapid variability of C1 are consistent with the range in measured surface brightness ratio if θ is in the range $\sim 50°$ – $\sim 80°$. The lower limit is derived from an apparent speed of 0.45c, $\alpha = -0.6$, and $R = 8$. The upper limit is derived from the maximum speed of 1c, $\alpha = -0.6$, and $R = 4$.

It is interesting to note that Skibo, Dermer, & Kinzer (1994) infer an angle to the

line of sight of 61°±5° assuming that the 50 keV – 10 MeV emission detected by OSSE is beamed radiation that is Compton scattered into our line of sight. Such a large angle between the jet and our line of sight is also consistent with the large-scale radio morphology of Centaurus A.

4.3. Implications for the FR-I class

Centaurus A is the nearest example of an FR-I radio galaxy. As such, the detailed investigations possible for this source will have important implications for the FR-I class.

FR-I radio galaxies have, in general, been shown to be asymmetric close to the core, gradually attaining a more symmetrical appearance on larger scales. This is emphasized by VLBI observations of FR-I sources which give high lower limits on jet-to-counterjet surface brightness ratios (Venturi et al. 1994), indicating that the jets in FR-I radio galaxies may be initially relativistic on the parsec-scale; few have been shown to have observable counterjets (3C338, Venturi et al. 1994; NGC 4261, Jones & Wehrle 1997)

VLBI observations of FR-I radio galaxies also show that the apparent motions of components in their jets range from sub-luminal (Venturi et al. 1994) to mildly superluminal (Pearson 1996). For the sub-luminal sources, if the simple assumption is made that the intrinsic jet speed, β_{jet}, is approximately equal to the observed speed of the components, β_{app}, then small jet angles to the line of sight are required to achieve high jet-to-counterjet brightness ratios and the intrinsic size of FR-I radio sources would have to be many times larger than their already large projected sizes (e.g. NGC 315; Venturi et al. 1993). To ease the requirement for extremely large intrinsic size, it has been suggested that the speed of components in parsec-scale jets does not reflect the true speed of the jet flows; the components are slow-moving patterns on an underlying relativistic flow. For example,

Bicknell (1994) suggests reverse shocks, advected along with the jet flow as a possible mechanism for producing slow-moving or even stationary features in parsec-scale FR-I jets.

This type of behavior has been seen in the two best studied FRI radio galaxies, M87 and Centaurus A. On the parsec-scale in M87 Biretta (1996) reports that the most prominent features in the jet move with significantly sub-luminal speeds over the long term, being perhaps consistent with stationary. However, on shorter time-scales the positions of components are somewhat chaotic, large regions of the jet brighten, and less prominent features appear to move rapidly. Biretta estimates apparent speeds in the jet of up to 2.5 c, applying similar arguments to those outlined in §4.1 to their observations.

In Centaurus A we have observed behaviors very similar to M87. We have seen that the slow $\sim$0.1c motions of components in the sub-parsec-scale jet persist in the long term but that the component C1 sometimes evolves on time-scales of months, leading to estimates for speeds much greater than 0.1c. For Centaurus A, however, we have an additional constraint on the parsec-scale jet since we have detected a counterjet. The slow long-term speeds in Centaurus A are not consistent with the observed range in jet-to-counterjet brightness ratio for any angle to the line of sight, an extreme example of the component speed - brightness ratio inconsistency noted for other FR-I radio galaxies (Venturi et al. 1994). However, the fast motions implied from the rapid variation of C1 are consistent with the appearance of the counterjet, which is in turn consistent with the large-scale morphology of the radio source. The presence of both fast (inferred) and slow (observed) speeds in Centaurus A and M87 may suggest that slow patterns exist in an underlying relativistic jet flow for FR-I radio galaxies on the parsec scale.

This suggestion has important implications for the difference between FR-I and FR-II radio galaxies. If it can be shown that both galaxy types have similar jet speeds on the parsec scale then differences in extended morphology and power may be more likely to be

caused by the kiloparsec-scale environment.

5. SUMMARY

We have presented VLBI images of Centaurus A with angular resolutions ranging between 1 and 14 milliarcseconds, over the frequency range 2.3 to 22.2 GHz, and spanning the period 1988 November to 1996 July. The images probe the structure of Centaurus A on sub-parsec scales.

Our model-fitting analyses of 8.4 GHz VLBI data have shown that the sub-parsec scale source consists of an inverted spectrum core component and a jet which contains three discrete components. These components have overall sub-luminal motions of approximately 0.1c. However, C1 appears to undergo short time-scale changes, perhaps reflecting a faster underlying jet speed of > 0.45c. The detection of a sub-parsec scale counterjet in Centaurus A with a jet-to-counterjet surface brightness ratio of 4 – 8 is inconsistent with a jet speed of 0.1 c. If the jet speed is taken as >0.45 c then the counterjet, the jet speed, and the large-scale radio and optical morphology of Centaurus A are consistent. This result for Centaurus A and similar results for M87, the other well-studied FR-I radio galaxy, may support a model for VLBI jets in which the commonly observed moving components are slow patterns on a much faster underlying jet flow.

There is some evidence that the core-component zero separation times for C1, C2, and C3 are linked to enhancements in the X-ray flux from Centaurus A. The X-rays are more likely to come from the core rather than from the more extended jet components.

We thank the participating observatories for their generous allocations of time over the eight-year period of investigation. We also thank the staff of the Caltech/JPL Block II correlator for their assistance in correlating the Mark II data. Part of this work

was undertaken while S.J.T. held a National Research Council - NASA/JPL Research Associateship. S.J.T. also acknowledges receipt of an Australian Postgraduate Award and the ATNF student program. Part of this work was carried out at the Jet Propulsion Laboratory, California Institute of Technology, under contract with the National Aeronautics and Space Administration. The Australia Telescope is funded by the Commonwealth of Australia for operation as a national facility managed by the CSIRO. The Astronomical Image Processing Software and the VLBA were developed and are maintained by the National Radio Astronomy Observatory which is operated by Associated Universities, Inc., under cooperative agreement with the National Science Foundation

REFERENCES

Bicknell, G.V. 1994, ApJ, 422, 542

Biretta, J. 1996, in Energy Transport in Radio Galaxies and Quasars, eds. P.E. Hardee, A.H. Bridle, and J.A. Zensus (San Fransisco: ASP), 187

Bolton, J.G., Stanley, G., and Slee, O.B. 1949, Nature, 164, 101

Bond, I.A. et al. 1996, A&A, 307, 708

Botti, L.C.L. and Abraham, Z. 1993, MNRAS, 264, 807

Burns, J.O., Feigelson, E.D., and Schreier, E.J. 1983, ApJ, 273, 128

Clarke, D.A., Burns, J.O., and Norman, M.L. 1992, ApJ, 395, 444

Combi, J.A. and Romero, G.E. 1997, A&A, 121, 11

Döbereiner, S. et al. 1996, ApJ, 470, L15

Hui, X., Ford, H.C., Ciardullo, R., & Jacoby, G.H. 1993, ApJ, 414, 463

Jauncey, D.L. et al. 1995, Proc.Nat.Acad.Sci.USA, 92, 11368

Jones, D.L. et al. 1996, ApJ, 466, L63

Jones, D.L. and Wehrle, A.E. 1997, ApJ, in press

Joy, M., Harvey, P.M., Tollestrup, E.V., Sellgren, K., McGregor, P.J., and Hyland, A.R. 1991, ApJ, 366, 82

Junkes, N., Haynes, R.F., Harnett, J.I., and Jauncey, D.L. 1993, A&A, 269, 29

Kellermann, K.I., Zensus, J.A., and Cohen, M.H. 1997, ApJ, 475, L93

Kinzer, R.L. et al. 1995, ApJ, 449, 105

Meier, D.L. et al. 1993, in 'Sub-arcsecond Radio Astronomy', eds. R.J. Davis & R.S. Booth (Cambridge: Cambridge University Press), 201

Meier, D.L. et al. 1989, AJ, 98, 27

Morini, M. et al. 1989, ApJ, 347, 750

Odenwald, S., Gehrels, N., and Howard, S. 1994, in IAU symposium 159, 'Multiwavelength continuum emision of AGN', (Eds T.J.-L. Courvoisier & A. Blecha: Kluwer), 323

Pearson, T.J. 1991, BAAS, 23, 991

Pearson, T.J. 1996, in Energy Transport in Radio Galaxies and Quasars, eds. P.E. Hardee, A.H. Bridle, & J.A. Zensus (San Fransisco: ASP), 97

Preston, R.A., Wehrle, A.E., Morabito, D.D., Jauncey, D.L., Batty, M.J., Haynes, R.F., and Wright, A.E. 1983, ApJ, 266, L93

Preston, R.A. et al. 1996, in IAU 175: Extragalactic Radio Sources eds. R. Ekers, C. Fanti, & L. Padrielli (Dordrecht: Kluwer), 21

Shepherd, M.C., Pearson, T.J., and Taylor, G.B. 1994, BAAS, 26, 987

Skibo, J.G., Dermer, C.D. and Kinzer, R.L. 1994, ApJ, 426, L23

Tingay, S.J. et al. 1994 Aust.J.Phys. 47, 619

Tornikoski, M. et al. 1996, A&ASupp 116, 157

Venturi, T. et al. 1993, ApJ, 408, 81

Venturi, T. et al. 1994, in The First Stromlo Symposium: The Physics of Active Galaxies (ASP conf. 54: Eds G.V. Bicknell, M.A. Dopita, and P.J. Quinn), 247

Wade, C.M., Hjellming, R.M., Kellermann, K.I., and Wardle, J.F.C. 1971, ApJ, 170, L11

This manuscript was prepared with the AAS LaTeX macros v4.0.

6. TABLE CAPTIONS

Table 1 The log of VLBI observations: *Column 1* contains the observing epoch. *Column 2* contains the observing frequency. *Column 3* contains the array configurations (S = SHEVE, V = VLBA) and the recording formats (II = Mark II, III = Mark III, V = VLBA) used at that epoch. *Column 4* lists the telescopes according to the codes listed below. *Column 5* contains the number of useful baselines and closure triangles from the observation used in the imaging process. *Column 6* contains the observation length, T.
Antenna codes: D43 = Tidbinbilla (70m), D45 = Tidbinbilla (34m), PA = Parkes (64m), HO = Hobart (26m), MP = Mopra (22m), AT = Narrabri (22m), AS = Alice Springs (26m), HH = Hartebeesthoek (26m), PR15 = Perth (15m), FD = Fort Davis (25m), OV = Owens Valley (25m), PT = Pie Town (25m), KP = Kitt Peak (25m), LA = Los Alamos (25m), MK = Mauna Kea (25m), SC = Saint Croix, SH = Shanghai (25m), PR27 = Perth (27m).

Table 2 Parameters of the VLBI maps: *Column 1* lists the figure number. *Column 2* gives the observing frequency. *Column 3* lists the observing epoch. *Column 4* lists the mapsize in pixels and cellsize in milliarcseconds. *Column 5* lists the peak flux density in the map in Jy/beam. *Column 6* lists the off source RMS noise level in the map in mJy/beam. *Column 7* lists the total flux density in the map in Jy. *Column 8* lists the restoring beam FWHM dimensions in milliarcseconds and position angles in degrees.

Notes to table 2

1. 2.3 GHz component of dual-frequency, simultaneous observations at this epoch.
2. Image produced from combining the VLBA and SHEVE array data at this epoch. No baselines between the VLBA and the SHEVE array (trans-Pacific) were used.
3. Image produced from only the SHEVE array data at this epoch.
4. Image has been shifted West 10 mas and South 10 mas.

5. 8.4 GHz component of dual-frequency, simultaneous observations at this epoch.

Table 3 Best fit models for low resolution 8.4 GHz data: *Column 1*, S, the integrated flux density of the model component in Jy. *Column 2*, d, the distance of the model component from the designated phase centre in milliarcseconds. *Column 3*, θ, the position angle of the model component centroid from the designated phase centre in degrees east of north. *Column 4*, A, the major axis extent of the model component in milliarcseconds. *Column 5*, B/A, the ratio of model component minor axis to major axis extent. *Column 6*, ϕ, the position angle of the model component major axis in degrees east of north. *Column 7*, Type, the type of model component. Type 1 components are elliptical Gaussians, in which case the component extents are the FWHM of the Gaussian. Type 2 components are elliptical disks of uniform surface brightness, in which case component extent is the full extent. This is a non-variable parameter in MODELFIT. *Column 8*, I.D., the component identification.

7. FIGURE CAPTIONS

Fig 1 Contour levels for a, b, d, e, g, i, j, n, o, p, q, r, s, t, and u are -1, 1, 2, 4, 8, 16, 32, and 64% of the peak flux density in the map as given in Table 1. The contour levels for f, h, k, l, m are -0.5, 0.5, 1, 2, 4, 8, 16, 32, and 64% of the peak flux densities as given in Table 1.

Fig 2 Montage of 8.4 GHz VLBI images. Left panel shows the series of clean component models from the 8.4 GHz SHEVE images. An average restoring beam of 9 × 3 mas in position angle −83° has been used for the SHEVE models. The right panel shows the series of clean component models from the 8.4 GHz VLBA images. An average restoring beam of 4 × 13 mas in position angle 2° has been used for the VLBA models. All models and beams have been rotated by 39°. Note that the two panels displayed have significantly different scales, due to the time-scales over which the observations were made.

Fig 3 Core – C1 (top) , core – C2 (middle) , and core – C3 (lower) separations as a function of time, from 8.4 GHz modelfitting analyses.

Fig 4 Comparison of 8.4 GHz models from 91/11/24 and 92/03/26. The horizontal axes are coordinate axes in milliarcseconds and the vertical axis is the flux density in Jy/beam (scale not shown, but is identical to the images in Figure 2).

Fig 5 8.4 GHz light curve for the Centaurus A parsec-scale components, as derived from the modelfitting results.

Epoch Y/M/D	Freq. GHz	Arr./For.	Antennas	Base./Clos.	T hrs
88/11/10	2.3	S/II	AT, MP, D43, D45, PA, HO, AS, HH	19/24	12
91/03/06	8.4	S/II	AT, D43, PA, HO	6/4	11
91/11/24	8.4	S/II	AT, MP, D43, PA, HO	10/10	11
92/03/26	8.4	S/II	AT, MP, D43, D45, PA, HO, HH	14/16	10
92/11/22	8.4	S/II, III	AT, MP, D43, PA, HO, PR15, HH	19/21	12
		V/II, III	SC, FD, LA, PT, KP, OV, MK		
92/11/25	4.8	S/II	AT, MP, PA, HO, SH, PR27, HH	9/7	12
93/02/16	4.8	S/II	AT, MP, PA, HO, PR27	9/7	12
93/07/03	8.4	S/II, III	AT, MP, D43, PA, HO, PR15, HH	23/23	12
		V/II, III	SC, FD, LA, PT, KP, OV		
93/10/20	8.4	S/II, III	AT, MP, D45, PA, HO, PR15, HH	25/30	12
		V/II, III	SC, FD, LA, PT, KP, OV, MK		
94/02/27	8.4	S/II	AT, MP, D43, D45, PA, HO	10/10	14
94/06/20	8.4	S/II	AT, MP, D45, PA, HO	10/10	13
95/07/03	2.3/8.4	V/V	SC, NL, FD, LA, PT, KP, OV, MK	18/20	4
95/11/17	22.2	V/V	SC, NL, FD, LA, PT, KP, OV, MK	10/10	4
96/03/23	8.4	V/V	SC, NL, FD, LA, PT, KP, OV, MK	10/10	5
96/04/30	8.4	V/V	SC, NL, FD, LA, PT, KP, OV, MK	15/20	5
96/06/02	8.4	V/V	SC, NL, FD, LA, PT, KP, OV, MK	10/10	5
96/07/01	8.4	V/V	SC, NL, FD, LA, PT, KP, OV, MK	10/10	4

Table 1:

Figure	Freq. GHz	Epoch Y/M/D	Map/Cell pixel/mas	Peak Jy/beam	Noise mJy/beam	S_{total} Jy	Beam mas/mas/°	Notes
1a	2.3	88/11/10	512/1	1.4	6	4.0	5.6/7.2/6.7	
1b	2.3	95/07/03	1024/1	1.0	3	7.1	2.5/6.5/-0.6	1
1c	4.8	92/11/25	512/0.4	0.7	3	4.8	2.6/3.1/-24.4	
1d	4.8	93/02/16	512/0.4	1.0	4	5.4	2.6/3.5/25.1	
1e	8.4	91/03/06	512/0.5	3.0	9	7.6	3.0/7.0/-81.3	
1f	8.4	91/11/24	512/0.5	2.6	6	7.8	3.1/7.2/-88.9	
1g	8.4	92/03/26	512/0.5	2.6	5	7.7	3.1/9.0/-81.3	
1h	8.4	92/11/22	512/0.25	1.6	2	9.6	1.8/2.2/4.7	2
1i	8.4	92/11/22	512/0.5	3.0	3	10.1	4.1/5.3/-56.3	3
1j	8.4	93/07/03	512/0.2	1.1	4	4.6	1.5/2.2/-5.8	2
1k	8.4	93/07/03	512/0.5	1.6	4	5.6	2.9/7.8/-74.7	3
1l	8.4	93/10/20	512/0.3	1.8	1	7.1	1.7/3.2/27.3	2,4
1m	8.4	93/10/20	512/0.5	2.4	5	7.6	3.2/6.8/-83.1	3
1n	8.4	94/02/27	512/0.5	2.6	7	6.8	3.2/6.3/-83.3	
1o	8.4	94/06/20	512/0.5	2.1	7	5.4	3.0/6.4/-84.2	
1p	8.4	95/07/03	512/0.5	2.0	6	6.0	2.3/12.2/-4.2	5
1q	8.4	96/03/23	512/0.5	1.7	4	5.3	2.4/13.6/-10.0	
1r	8.4	96/04/30	512/0.5	2.1	4	5.2	3.0/13.5/9.8	
1s	8.4	96/06/02	512/0.5	2.1	4	5.1	3.1/13.3/8.1	
1t	8.4	96/07/01	512/0.5	1.8	4	4.3	3.1/13.0/6.6	
1u	22.2	95/11/17	512/0.1	2.4	6	4.0	1.2/5.3/8.6	

Table 2:

S (Jy)	d (mas)	$\theta°$	A (mas)	B/A	$\phi°$	Type	I.D.
91/03/06							
2.34	0.00	0.0	2.94	0.00	73.6	1	Core
2.93	3.47	53.1	2.62	0.27	66.9	1	C2
1.65	14.39	49.5	4.08	0.68	52.4	1	C1
0.73	22.97	51.3	3.94	0.15	21.8	1	Jet?
91/11/24							
2.18	0.00	0.0	2.74	0.11	37.6	1	Core
2.75	4.35	51.2	2.84	0.53	42.6	1	C2
1.22	12.79	52.2	4.59	0.32	41.5	1	C1/Jet?
1.47	20.46	49.1	12.58	0.00	47.1	1	C1/Jet?
0.60	32.54	49.5	35.02	0.00	46.5	2	Jet
92/03/26							
2.40	0.00	0.0	2.04	0.00	62.1	1	Core
1.83	4.75	51.7	2.30	0.00	65.7	1	C2
3.02	15.92	49.5	9.86	0.17	47.8	1	C1
1.02	28.15	51.5	32.90	0.00	45.1	2	Jet
92/11/22							
3.31	0.00	0.0	2.90	0.18	50.8	1	Core
1.17	6.35	50.5	3.17	0.00	56.4	1	C2
1.05	16.96	47.9	5.42	0.00	32.8	1	C1
4.53	14.4	50.4	37.4	0.00	48.7	2	Jet

Table 3:

S (Jy)	d (mas)	$\theta°$	A (mas)	B/A	$\phi°$	Type	I.D.
93/07/03							
2.30	0.00	0.0	3.65	0.00	49.6	1	Core
0.69	6.34	46.3	7.76	0.31	69.7	1	C2
0.26	16.46	56.6	6.45	0.00	0.11	1	C1/Jet?
0.52	22.53	49.9	3.77	0.00	55.2	1	C1/Jet?
1.93	15.00	50.2	25.96	0.14	49.9	1	Jet
93/10/20							
2.35	0.00	0.0	1.86	0.00	56.5	1	Core
1.05	3.16	49.1	0.00	0.00	00.0	1	C3
1.20	8.36	52.4	6.91	0.00	54.1	1	C2
2.39	22.69	50.3	13.7	0.00	45.4	1	C1
0.71	42.54	50.4	19.37	0.12	45.2	1	Jet
94/02/27							
3.26	0.00	0.0	3.20	0.00	60.1	1	Core
0.36	3.60	40.8	0.00	0.00	00.0	1	C3
1.21	10.27	52.3	6.00	0.00	43.6	1	C2
1.39	22.82	49.3	6.83	0.17	45.8	1	C1
0.73	35.00	50.6	20.1	0.11	46.5	1	Jet
94/06/20							
1.97	0.00	0.0	2.04	0.00	45.8	1	Core
1.05	2.91	50.6	1.58	0.68	31.5	1	C3
0.81	9.44	47.3	9.09	0.00	48.1	1	C2
0.78	16.31	53.5	38.22	0.00	47.7	1	Jet
0.87	24.20	49.0	9.38	0.19	57.3	1	C1

S (Jy)	d (mas)	θ°	A (mas)	B/A	ϕ°	Type	I.D.
95/07/03							
2.82	0.00	0.0	2.62	0.70	35.9	1	Core
1.39	4.51	44.7	3.15	0.77	148.4	1	C3
0.89	11.04	52.5	4.80	0.49	52.8	1	C2
1.04	23.36	50.88	11.00	0.11	34.2	1	C1
96/03/23							
2.44	0.00	0.0	2.94	0.00	54.3	1	Core
1.04	3.79	43.7	3.15	0.82	-54.7	1	C3
1.04	10.07	51.7	12.56	0.43	25.9	1	C2
0.89	23.57	52.5	12.47	0.38	50.4	1	C1
96/04/30							
2.38	0.00	0.0	2.77	0.51	50.7	1	Core
1.08	4.94	50.4	3.40	0.43	58.0	1	C3
0.72	12.37	52.6	8.05	0.27	30.1	1	C2
0.83	24.81	52.0	11.42	0.11	48.5	1	C1
96/06/02							
2.35	0.00	0.0	2.62	0.60	43.5	1	Core
1.05	5.31	50.0	3.09	0.00	74.4	1	C3
0.81	12.16	52.6	6.89	0.29	32.9	1	C2
0.99	24.69	51.9	13.75	0.27	35.0	1	C1
96/07/01							
2.03	0.00	0.0	2.64	0.17	51.7	1	Core
0.79	5.02	51.8	2.86	0.00	58.7	1	C3
0.84	12.40	53.3	8.97	0.34	24.8	1	C2
0.79	25.92	50.7	13.73	0.26	34.5	1	C1

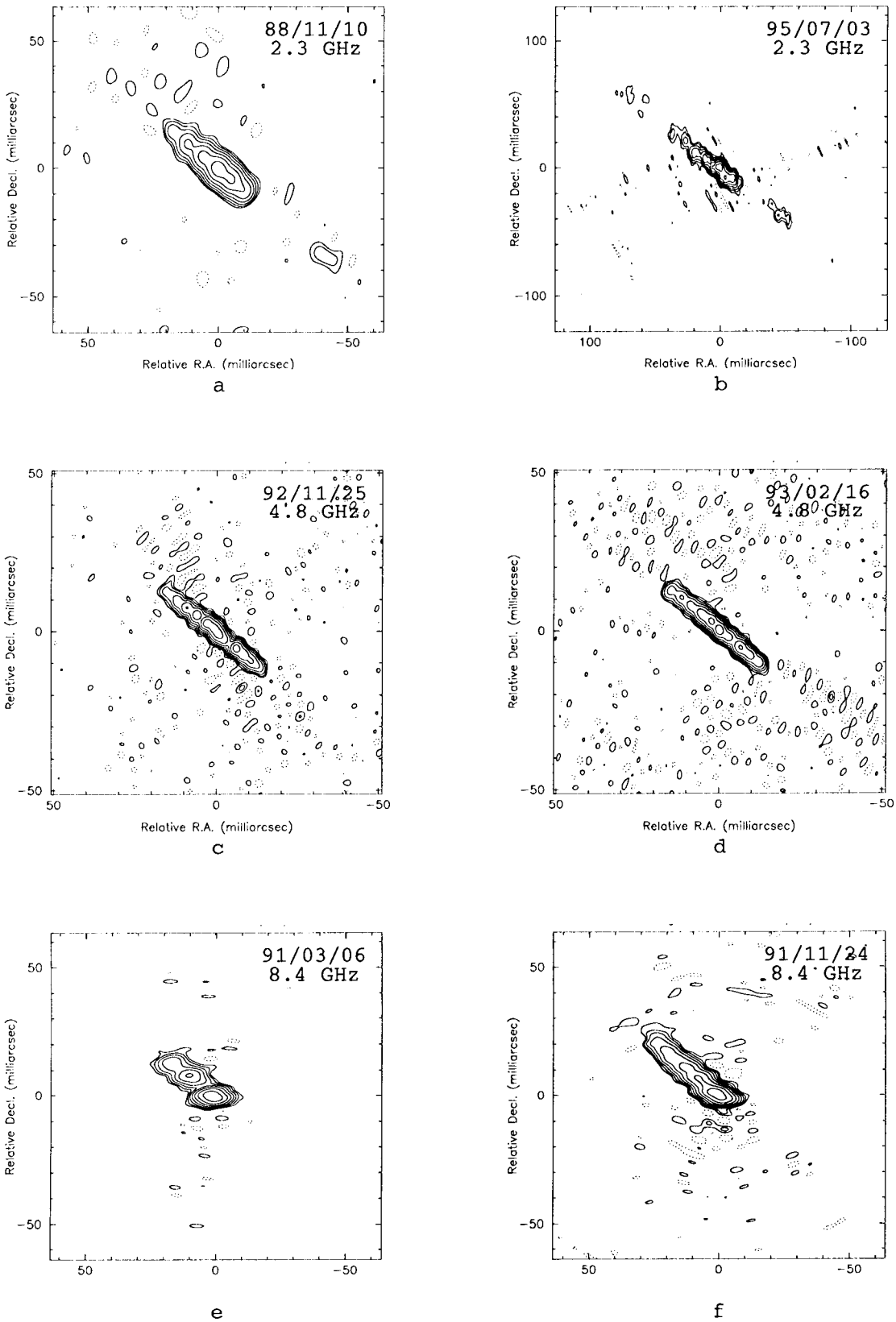
88/11/10
2.3 GHz
95/07/03
2.3 GHz
92/11/25
4.8 GHz
93/02/16
4.8 GHz
91/03/06
8.4 GHz
91/11/24
8.4 GHz
Relative Decl. (milliarcsec)
Relative R.A. (milliarcsec)
a
b
c
d
e
f

FIGURE 1

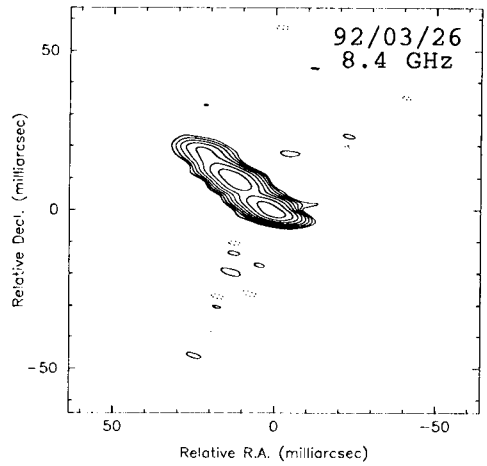

g

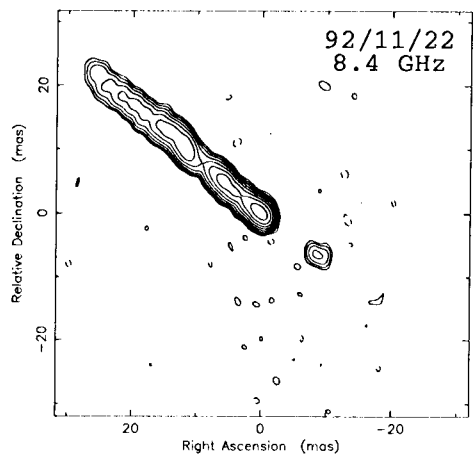

h

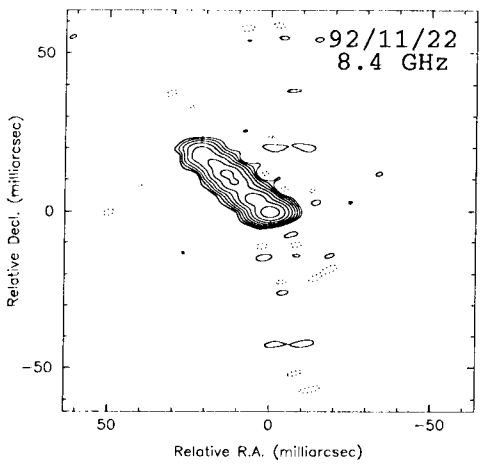

i

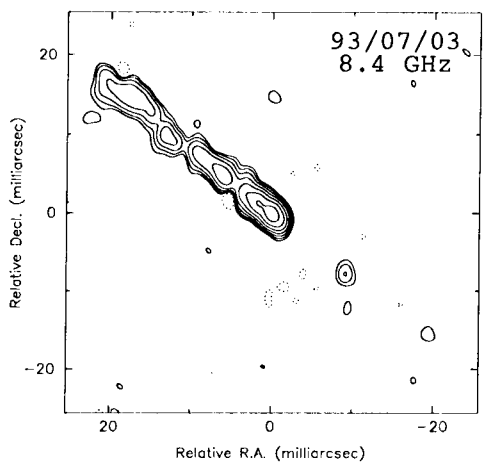

j

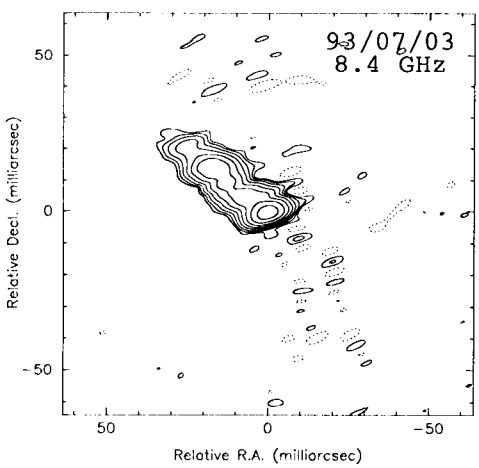

k

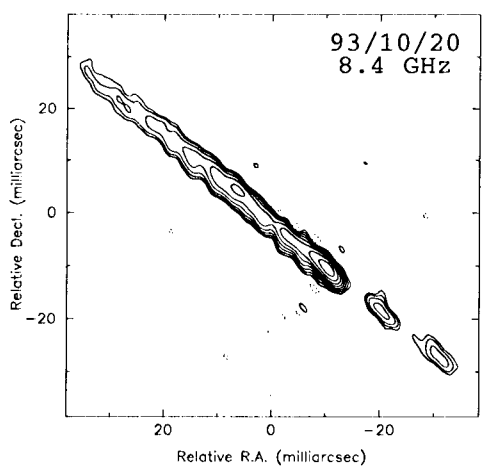

l

FIGURE 1 - cont

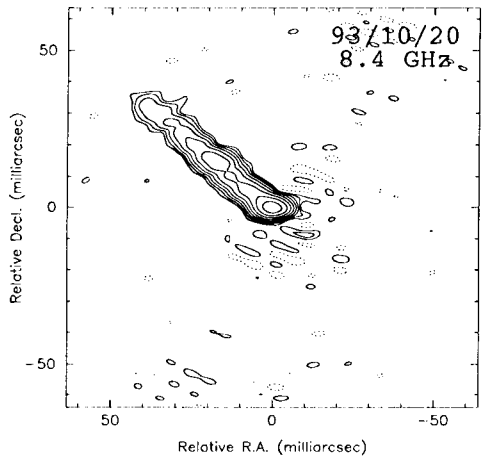

m

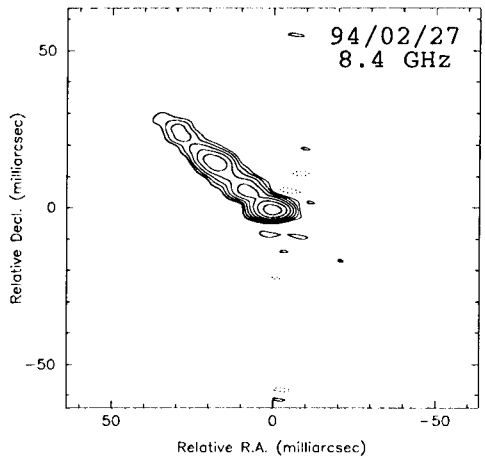

n

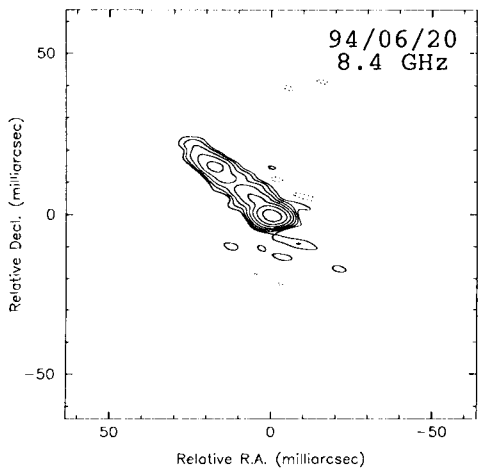

o

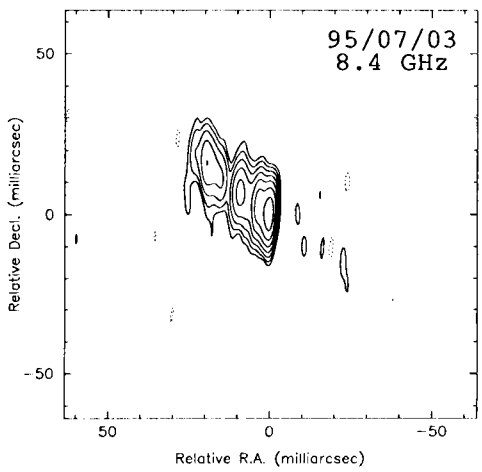

p

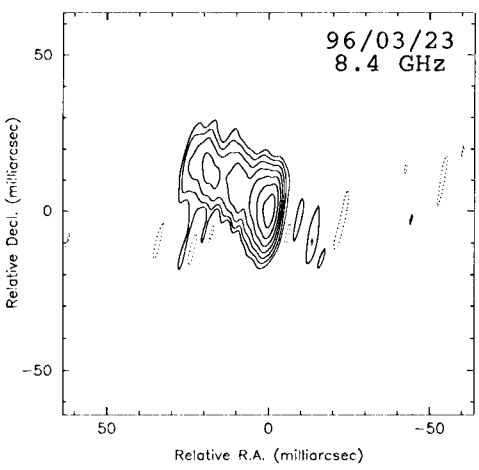

q

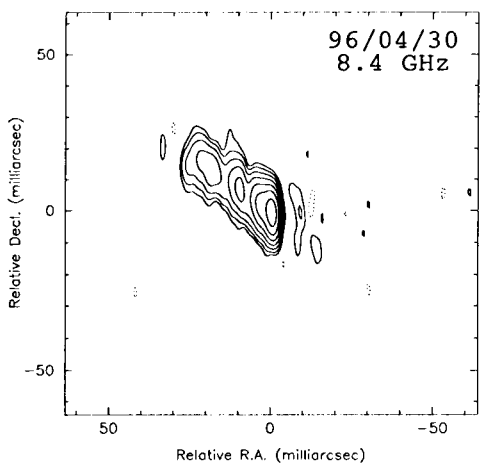

r

FIGURE 1 - cont

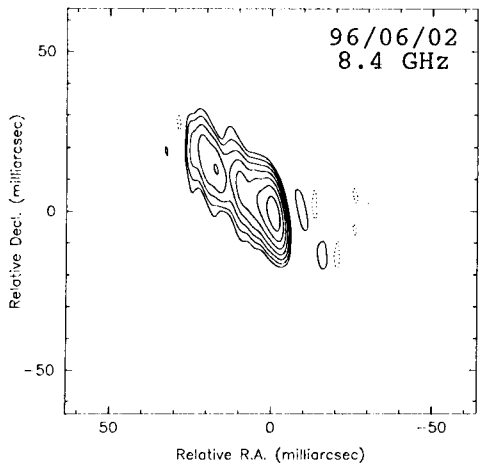

s

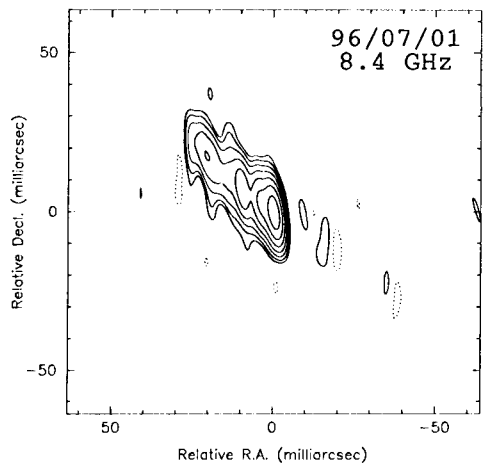

t

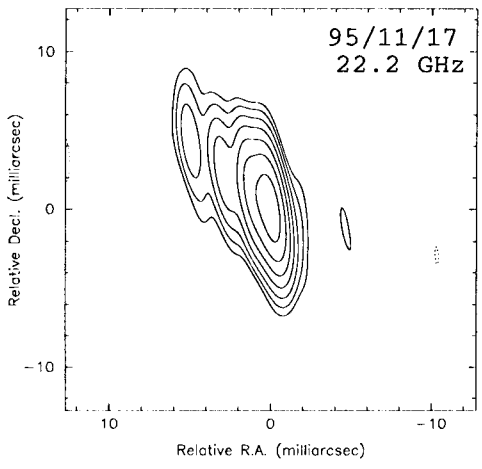

u

FIGURE 1 - cont

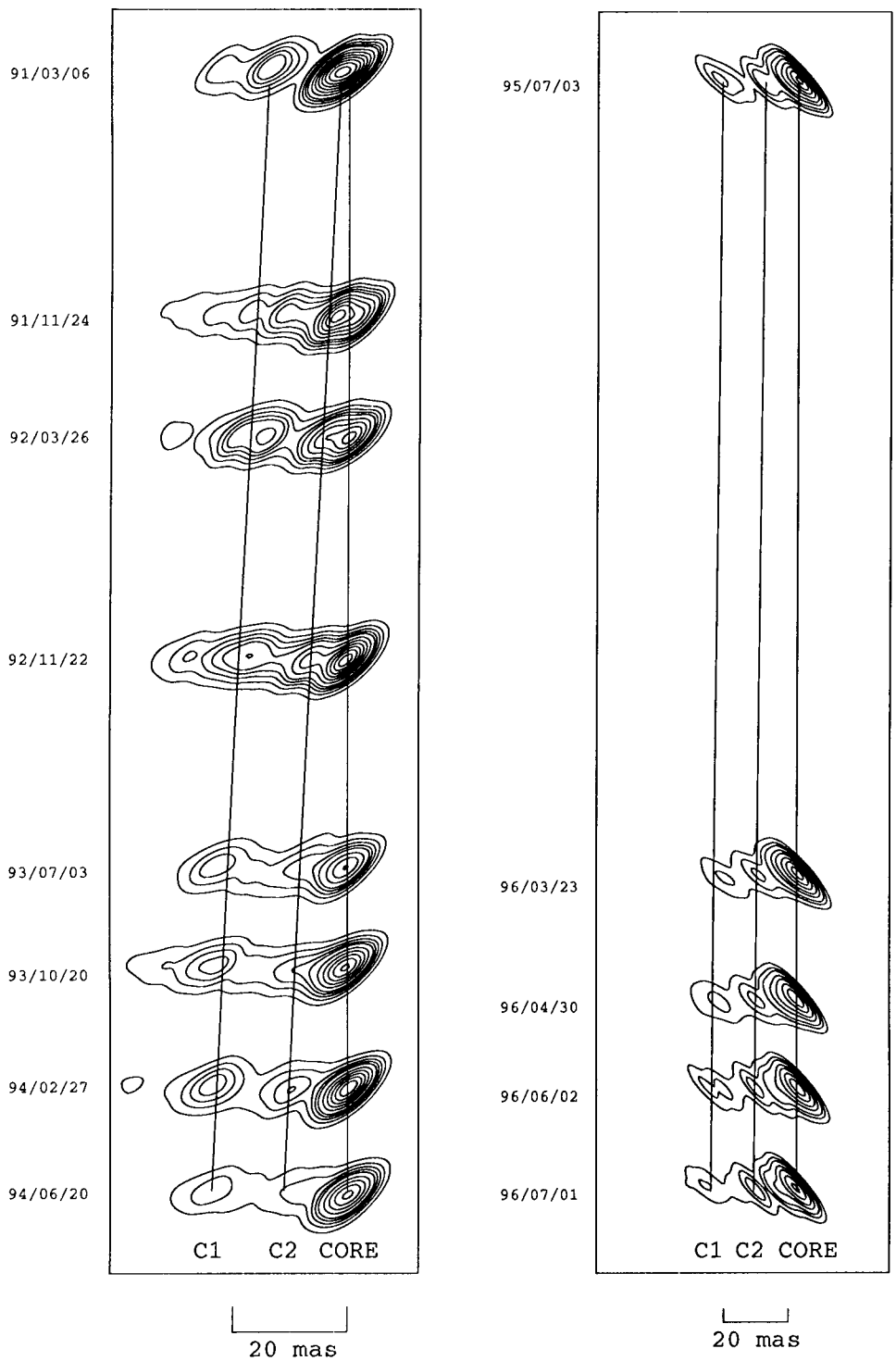
91/03/06
91/11/24
92/03/26
92/11/22
93/07/03
93/10/20
94/02/27
94/06/20
C1 C2 CORE
20 mas
95/07/03
96/03/23
96/04/30
96/06/02
96/07/01
C1 C2 CORE
20 mas

Fig. 2.—

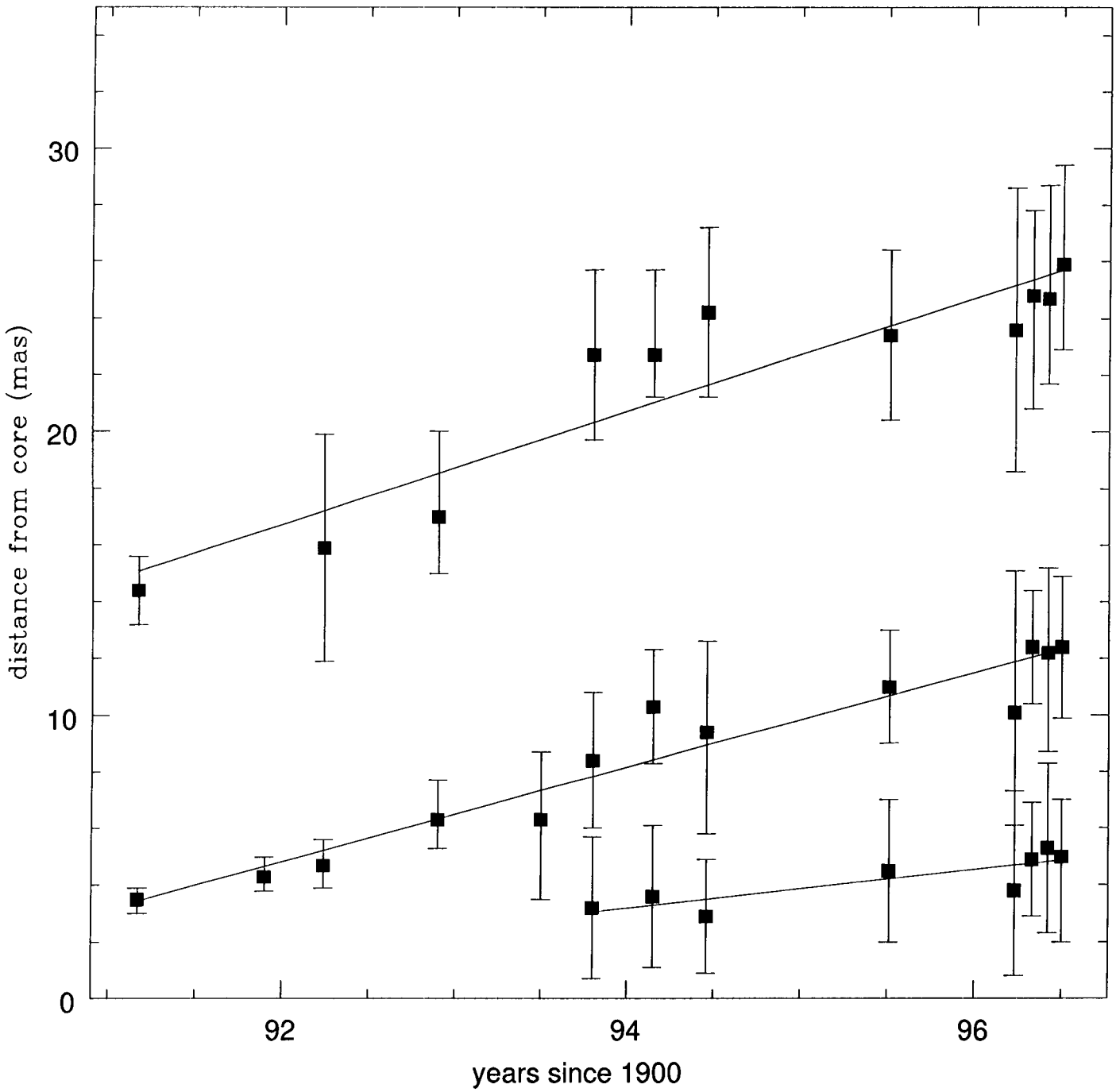

Fig. 3.—

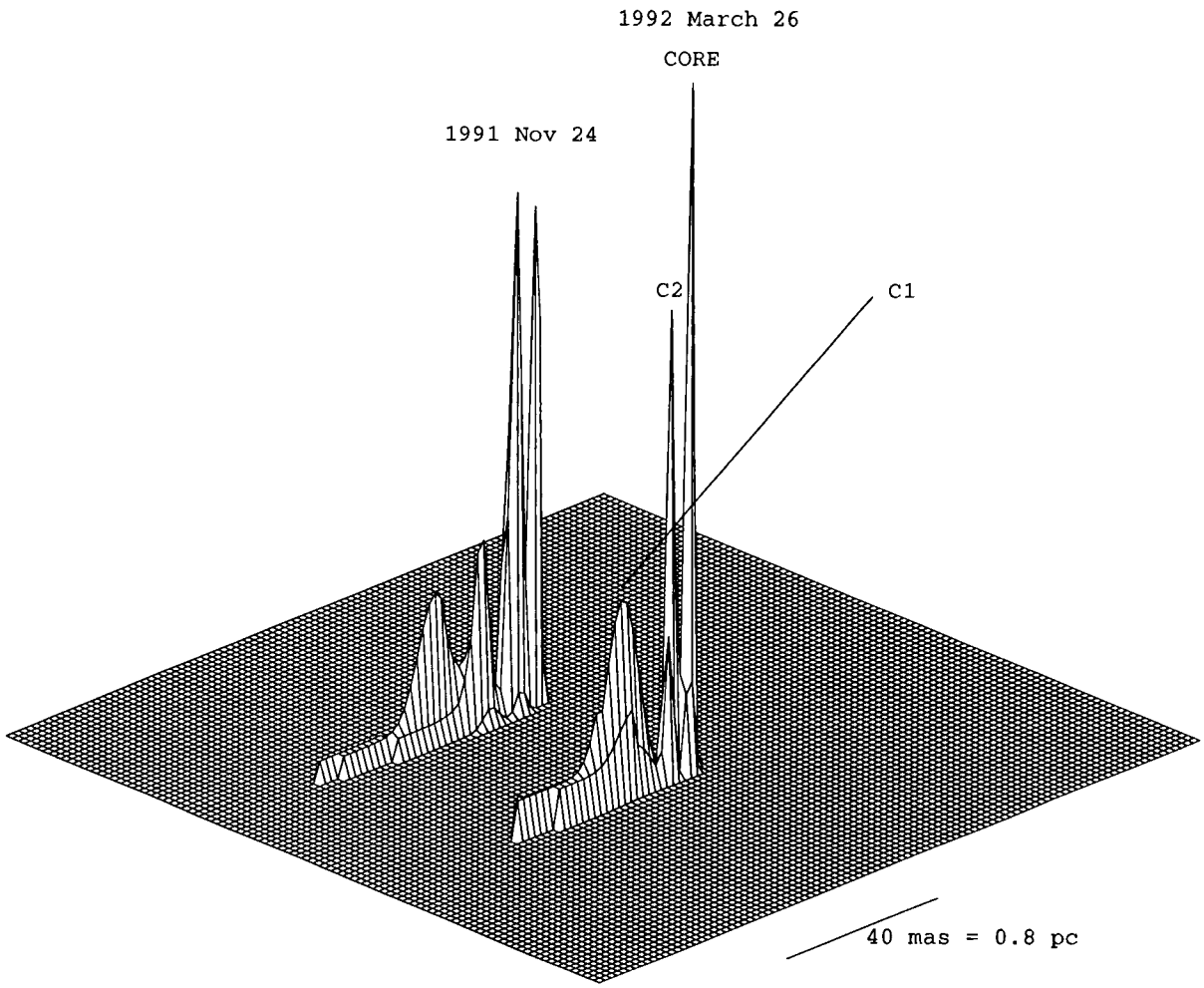

Fig. 4.—

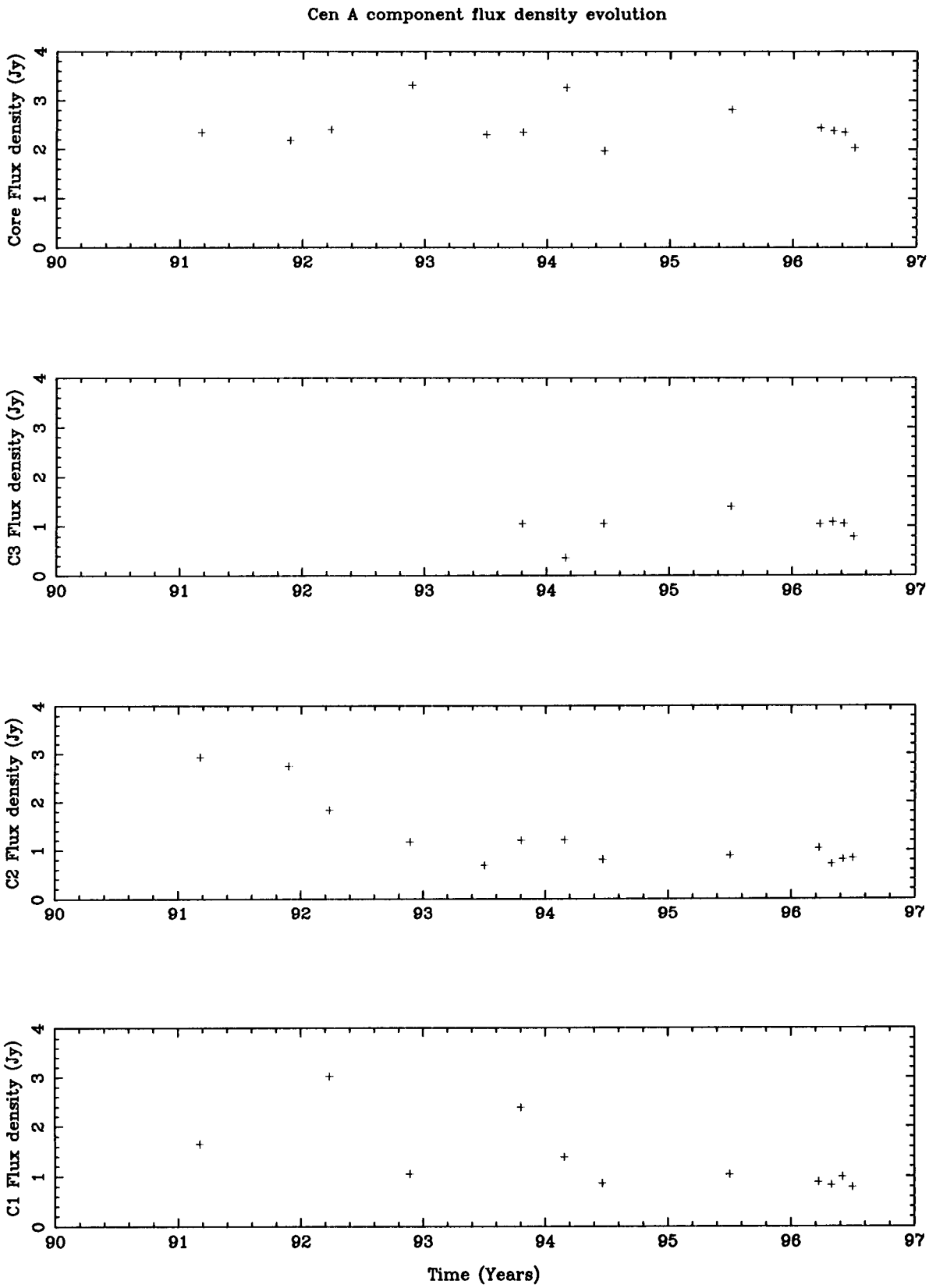
Cen A component flux density evolution
Core Flux density (Jy)
C3 Flux density (Jy)
C2 Flux density (Jy)
C1 Flux density (Jy)
0
1
2
3
4
90
91
92
93
94
95
96
97
Time (Years)

Fig. 5.—